Pressure influence on the valence and magnetic state of Yb ions in noncentrosymmetric heavy-fermion YbNiC2

D A Salamatin, V A Sidorov, N M Chtchelkatchev, M V Magnitskaya, N Martin, A E Petrova, L N Fomicheva, Jing Guo, Cheng Huang, Yazhou Zhou, et al.

Pressure influence on the valence and magnetic state of Yb ions in noncentrosymmetric heavy-fermion $YbNiC_2$

D. A. Salamatin,[1,2,3] V. A. Sidorov,[1,3] N. M. Chtchelkatchev,[1] M. V. Magnitskaya,[1,3] N. Martin,[4] A. E. Petrova,[1,3] L. N. Fomicheva,[1] Jing Guo,[5] Cheng Huang,[5] Yazhou Zhou,[5] Liling Sun,[5] and A. V. Tsvyashchenko[1,3,*]

[1]*Institute for High Pressure Physics, Russian Academy of Sciences, 14 Kaluzhskoe shosse, 108840 Troitsk, Russia*

[2]*Joint Institute for Nuclear Research, 141980 Dubna, Moscow Region, Russia*

[3]*P.N. Lebedev Physical Institute of the Russian Academy of Sciences, 53 Leninskiy prospekt, 119991 Moscow, Russia*

[4]*Université Paris-Saclay, CNRS, CEA, Laboratoire Léon Brillouin, 91191 Gif-sur-Yvette, France*

[5]*Institute of Physics, Chinese Academy of Sciences, 100190 Beijing, People's Republic of China*

(Received 19 January 2021; revised 25 May 2021; accepted 1 June 2021; published 16 June 2021)

We present studies of neutron diffraction, electrical resistivity, magnetic susceptibility, magnetization, and specific heat of noncentrosymmetric $YbNiC_2$. At normal pressure, $YbNiC_2$ is a moderate heavy-fermion compound with Kondo lattice. At 16 K we observe an anomaly in the temperature dependence of specific heat which is ascribed to an abrupt valence change of Yb ions. At pressures above 7 GPa, the valence change and the Kondo lattice state are suppressed, and near a temperature of 10 K we detect the appearance of magnetic order. Above 5 GPa, the temperature dependence of the resistivity behaves similarly to other compounds of the $CeNiC_2$-type family, indicating the formation of charge density waves. This is attributed to the nesting properties of the Fermi surface (FS) found within the density functional theory + dynamical mean field theory treatment. Our *ab initio* calculations also show that the valence of Yb in $YbNiC_2$ at normal conditions is 2.85, which increases with temperature and pressure. The FS of $YbNiC_2$ is anisotropic in shape in comparison with the 3D surface of $YbCoC_2$.

DOI: 10.1103/PhysRevB.103.235139

I. INTRODUCTION

Investigations of heavy-fermion (HF) systems with strong $4f$- and $5f$-electron correlations have attracted great interest among the condensed matter community for decades [1–7]. A wide variety of nontrivial phenomena has been observed in these systems, such as the coexistence of triplet superconductivity and ferromagnetism, localized and delocalized f electrons (dualism), the presence of valence fluctuations, magnetic interactions, and Kondo effect. The HF systems are highly sensitive to the pressure, magnetic fields and electron concentration, allowing us to change the state on the phase diagram. A special place among the systems is occupied by the intermetallic compounds of ytterbium (Yb) [8–10].

Usually, Yb-based intermetallic compounds have electronic instability of $4f$ electrons. The compounds are considered as hole analog of Ce-based compounds. The latter are fairly well studied experimentally and theoretically. At the same time, compounds with Yb are less studied. One of the reasons for this are the difficulties in synthesizing of Yb compounds at normal pressure due to the low melting point and high vapor pressure of Yb. In Yb-based compounds with d-transition metals and p-elements, Yb ions can be in a mixed-valent state [with two electronic configurations of Yb: Yb^{2+} with 14 ($4f^{14}6s^2$) and Yb^{3+} with 13 ($4f^{13}5d^16s^2$) electrons on the $4f$ shell] with strong electronic correlations, the description of which is still a problem without a general solution. At the same time, the knowledge of Yb valence behavior is a required ingredient in the understanding of the physics of competition between interactions arising in such systems. In Yb-based HF systems the applying of pressure results in a less pronounced change in interaction strength J between conduction and local f electrons (c-f) in comparison with Ce HF systems [9]. The external pressure is the best way to change the Yb valence and the balance between magnetic Ruderman-Kittel-Kasuya-Yosida (RKKY) and Kondo interactions.

In most cases the Yb valence in intermetallic compounds changes smoothly with temperature without the visible anomalies on the macroscopic quantities. A sharp isostructural valence transition was recently detected in $YbPd_2Al_3$ at $T = 110$ K with a change in the valence of Yb ions from 3^+ to 2^+ [11]. A valence crossover near quantum critical point was observed for $YbNi_3Ga_9$ compound [7,12]. $YbInCu_4$ is a well-known example of a HF system with the complex nature of concurrent low-lying states. There, at $T_v = 42$ K, the first-order valence transition (FOVT) is observed. As the temperature decreases, the Yb ion undergoes a transition from the approximately trivalent magnetic state to an intermediate valent state with a valence close to 2.8 [2,13] (arguably such a valence transition is similar to the α-γ transition in Ce and black-gold transition in SmS [14–16]). At $P > 2.4$ GPa, when FOVT is suppressed, the trivalent state of Yb becomes more energetically favorable, and $YbInCu_4$ becomes ferromagnetic at $T_M \approx 2.4$ K [17–19].

*tsvyash@hppi.troitsk.ru

It is known that the electronic and magnetic properties of Yb strongly depend on the properties of its partner [3,20–28]. In Ref. [29], it was shown that in the HF noncentrosymmetric (NC) $YbCoC_2$, $4f$ electrons are both in the localized and in the itinerant states with strong $3d$ Co electrons hybridization. This notably manifests in the high temperature of antiferromagnetic ordering. In this regard, it seemed interesting to study the isostructural $YbNiC_2$ compound and to trace how the properties of the $4f$ electrons of Yb are changed if the number of $3d$ electrons is increased by one.

The family of NC carbides $RNiC_2$ (where R is a rare-earth element) is studied intensively. The many nontrivial phenomena have been observed in them, such as quantum critical behavior, interplay of charge density wave (CDW), magnetism, and unconventional superconductivity [30–38]. The compounds with R = Nd, Tb, Dy, Ho, Er, and Tm order antiferromagnetically at low temperatures [39,40]. The Ni ions are nonmagnetic in the all-studied $RNiC_2$ compounds [40,41].

In this paper, we report on the high-pressure sample synthesis and study of the magnetic, heat, and transport properties of $YbNiC_2$. After an introduction to the experimental methods (Sec. II), we describe the ambient pressure properties of $YbNiC_2$. These include a transition from an approximately trivalent state to an intermediate valent state of Yb and the formation of a Kondo lattice with the decrease of temperature (Sec. III). Using pressure as a clean way to tune the valence state of Yb ions and change the RKKY and Kondo interaction strengths, we show that a magnetic ground state is reached above ≈7 GPa, when the trivalent state of Yb ions is recovered. Also, a pressure-induced CDW is observed (Sec. IV). Our experimental findings are supplemented by extensive *ab initio* calculations, which confirm the valence state and magnetic transitions and reveal the peculiarities of the Fermi surface (FS) of $YbNiC_2$, supporting the formation of a CDW (Sec. V). The conclusions drawn from our experimental and numerical results are finally discussed in Sec. VI.

II. SAMPLE SYNTHESIS AND EXPERIMENTAL TECHNIQUES

Polycrystalline samples of $YbNiC_2$ were synthesized by melting Yb, Ni, and C (see Ref. [42]) at 8 GPa and 1500–1700 K using Toroid high-pressure cell. The purities of constituent elements were 99.7% for Yb, 99.9% for Ni, and 99.99% for C.

X-ray powder diffraction (XRPD) measurements at room temperature and ambient pressure were performed using the diffractometer Guinier camera G670, Huber (Cu-Kα_1).

The heat-capacity measurements at ambient pressure were performed using the PPMS, the measurements under the external magnetic field and high pressure were performed using modulation calorimetry (ac-calorimetry) [43,44]. Measurements below 5 GPa were performed in a miniature clamped Toroid-type device with glycerine-water (3:2) liquid as the pressure-transmitting medium [45]. Measurements in the range 2.5–9.5 GPa were performed in a clamped Bridgman anvil device with a solid pressure medium. The electrical resistivity measurements were performed on bulk polycrystalline samples using a Toroid-type device up to 5 GPa and a diamond anvil cell (DAC) with NaCl as a pressure medium at higher pressures. At hydrostatic pressure the resistivity measurements were performed on the samples polished to the shape of rectangular bars with typical dimensions 1.2 × 0.3 × 0.2 mm. Four platinum wires 25 μm in diameter were spot-welded to the sample. Samples used in a DAC have a shape of thin chips ≈250 μm in length. Four platinum foil electrodes were pressed to the sample in this case. The pressure for measurements in the DACs was determined by the ruby fluorescence method [46].

The neutron powder diffraction (NPD) patterns and small-angle neutron scattering (SANS) data were obtained on the G4-1 and PA20 [47] beamlines, respectively (Laboratoire Léon Brillouin, Saclay, France). The XRPD and NPD patterns were analyzed with the Rietveld method using FULLPROF software suite [48].

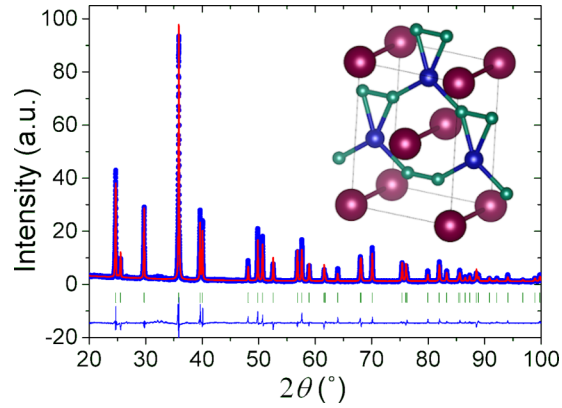

FIG. 1. The refined XRPD pattern for $YbNiC_2$ at T = 295 K and P = 0 GPa (the obtained lattice parameters are listed in Table I). The experimental points (blue dots), the calculated profiles (red line), and their differences (blue line) are shown. The bars in the lower part of the graph represent the calculated Bragg reflections that correspond to $YbNiC_2$. Inset: $YbNiC_2$ crystal structure with the red, blue, and green balls corresponding to Yb, Co, and C ions, respectively.

III. AMBIENT PRESSURE PROPERTIES

We begin the discussion from the results obtained at ambient pressure. $YbNiC_2$ crystallizes in NC orthorhombic $CeNiC_2$-type structure (space group *Amm*2, No. 38) in which alternating Yb and Ni planes are stacked along the c crystallographic direction, while carbon ions form dimers (Fig. 1). The refined crystal structure parameters at T = 295 K of the $YbNiC_2$ compound synthesized by us are given in Table I.

TABLE I. The crystallographic parameters of high-pressure synthesized $YbNiC_2$ (space group *Amm*2) obtained from XRPD data at T = 295 K, P = 0 GPa.

Lattice constant (Å)	a = 3.476	b = 4.494	c = 5.998
Atom position (r.l.u.)	x	y	z
Yb	0	0	0
Ni	1/2	0	0.603
C	1/2	0.157	0.295

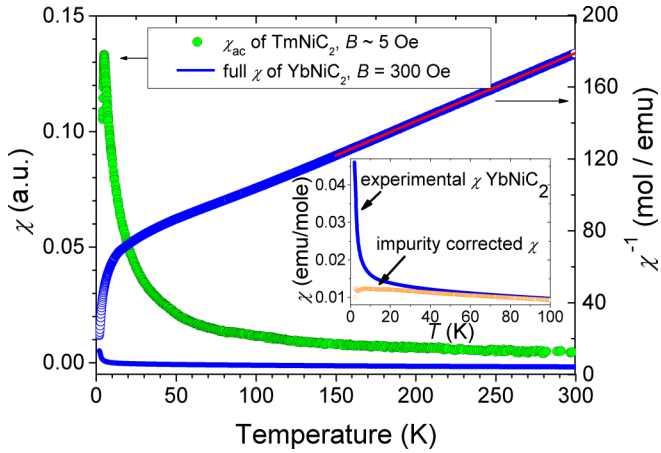

FIG. 2. The temperature dependencies of the magnetic susceptibility of $YbNiC_2$ measured in the external magnetic field $B = 300$ Oe (blue line and dots) together with the Curie-Weiss fit above 150 K (red line) and the magnetic susceptibility of $TmNiC_2$ measured in the external magnetic field $B = 5$ Oe (green dots). Inset: The experimental magnetic susceptibility of $YbNiC_2$ together with the impurity corrected part (orange dots).

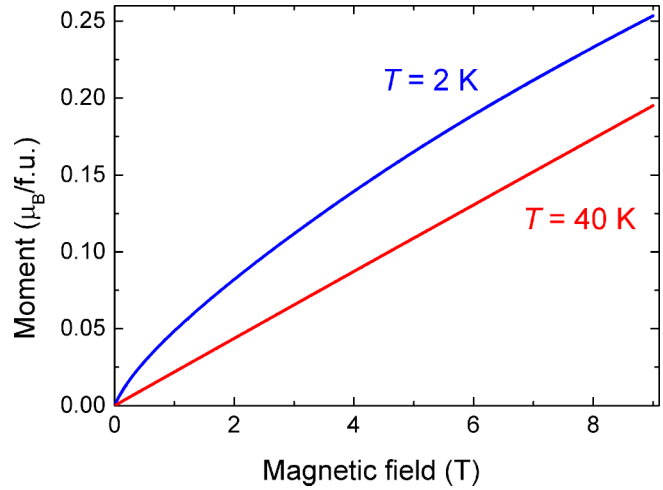

FIG. 3. The isothermal magnetization of $YbNiC_2$ measured in the field range $H = 0$–9 T at $T = 2$ and 40 K.

It should be noted that the unit cell volume (93.686 Å^3) deviates from the linear behavior observed through the $RNiC_2$ series [49]. Namely, it is larger than expected, which might already indicate an intermediate valence state of the Yb ions in $YbNiC_2$, since the size of Yb^{2+} is larger than that of Yb^{3+}.

The temperature dependence of the magnetic susceptibility for $YbNiC_2$ measured in an external magnetic field of 300 Oe above 150 K can be well approximated using the Curie-Weiss law with parameters $C = 2.633(2)$ emu K/mol and $\Theta_{CW} = -170.9(1)$ K (Fig. 2). The effective magnetic moment determined from C, $\mu_{eff} = 4.59(6)$ μ_B/f.u., nearly equals to the magnetic moment for the free Yb^{3+} ion (=4.54 μ_B). The large negative value of Θ_{CW} points to the $c - f$ hybridization. The upturn of the magnetic susceptibility at low temperature could be connected with the small amount (about 1.3%) of impurities (see the inset of Fig. 2). The possible impurity is $YbNi_5$ which orders ferromagnetically below 0.55 K [50]. The absolute value of the magnetic susceptibility of $YbNiC_2$ is in one order of magnitude smaller in comparison with the magnetic $RNiC_2$ compounds (see the measured magnetic susceptibility of the high pressure-high temperature synthesized $TmNiC_2$ compound which orders antiferromagnetically below $T_N \approx 5$ K [35] in Fig. 2).

The isothermal magnetization at $T = 40$ K, $M(H)$ has a smooth linear character, typical of a paramagnet (see Fig. 3). The magnetization measured at $T = 2$ K has a slight curvature and becomes linear for the fields above 7 T. The $\chi = M/H$ value from this linear part is equal to 0.008 emu/mol, which can probably be attributed to the spin fluctuations at low temperatures, as will be discussed later.

The temperature dependence of electrical resistivity reveals the metallic character of $YbNiC_2$ in the temperature range 100–350 K (see Fig. 4). At lower temperatures, the resistivity increases, reaching a maximum at $T_{max} = 18.0(3)$ K. In the temperature range 19–80 K, the resistivity is well described by the function $\rho_0 + c_{ph}T + c_K ln(T)$, where the first term is due to the temperature-independent scattering on static inhomogeneities of the lattice and disordered magnetic moments, the second temperature-linear term is due to the phonon scattering, and the last term is due to spin-flip scattering on Kondo impurities. The fitted parameters are $\rho_0 = 1.313(5)$ mΩ-cm, $c_{ph} = 3.24(6)$ μΩ-cm/K, and $c_K = -0.255(2)$ mΩ-cm. Such logarithmic behavior is similar to that observed in other Kondo lattices and the decrease of the resistivity at $T < T_{max}$ is due to the formation of coherence regime in the Kondo lattice.

The zero magnetic field-specific heat in the temperature range of 20–40 K can be well approximated by $\gamma_{HT}T + \beta_{HT}T^3$ function (see Fig. 5), where the first term is related to the electronic and the second to the phonon contributions to the specific heat. The fit parameters are $\gamma_{HT} = 174(2)$ mJ/mol-K^2 and $\beta_{HT} = 110(20)$ μJ/mol-K^4. The obtained Sommerfeld coefficient is close to the value for $YbCoC_2$ above the AFM transition temperature [29] ($\gamma = 190(1)$ mJ/mol-K^2). The Debye temperature Θ_D asso-

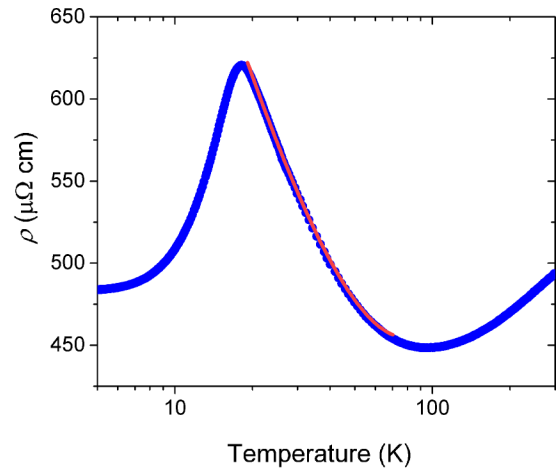

FIG. 4. The temperature dependence of the electrical resistivity of $YbNiC_2$ at $P = 0$ GPa (blue points). The red line is a fit (see text for the details).

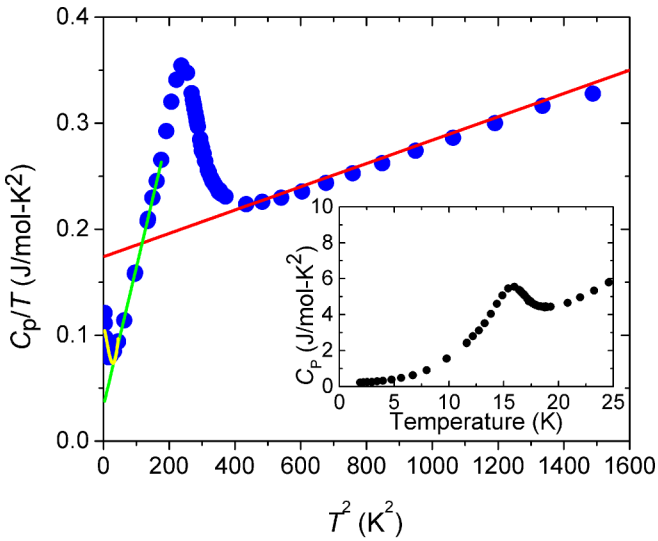

FIG. 5. Temperature dependence of the heat capacity of $YbNiC_2$ at $P = 0$ GPa and $H = 0$ T. The red line is a fit of the full heat capacity above the peak with $\gamma_{HT}T + \beta_{HT}T^3$ law, the green line is a fit of the full heat capacity below the peak by $\gamma_{LT}T + \beta_{LT}T^3$ law, and the yellow line is a fit of C_{4f} heat capacity below 7 K by $\gamma T + DT^3 ln(T/T_{sf})$ law. Inset: Full heat capacity.

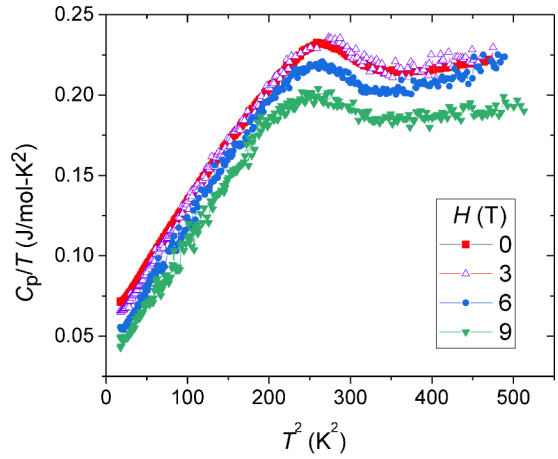

FIG. 6. Temperature dependence of the heat capacity of $YbNiC_2$ at different magnetic fields $H = 0 - 9$ T and $P = 0$ GPa.

ciated with β_{HT} as $\beta_{HT} = \frac{12\pi^4/5nR}{\Theta_D^3}$ is $\Theta_D = 413$ K. From a comparison with the specific heat of $LuNiC_2$ [36], the main part of the specific heat of $YbNiC_2$ below 40 K stems from $4f$ contribution as in the case of $RNiC_2$ with R = Ho, Er, Dy [51]. It may be attributed to the Schottky part of $(2J + 1)$-multiplet split in the crystal field.

The temperature dependence of the specific heat exhibits an anomaly with a maximum at $T \approx 16$ K. The size of the jump is equal to 2.35 J/mol-K, which is significantly smaller in comparison with the theoretical jump even for amplitude-modulated magnetic transition structure and the experimental specific- heat jumps at Neel temperature for $YbCoC_2$ [29], $HoNiC_2$ and $ErNiC_2$ [51].

The low-temperature part of the specific heat ($T < 13$ K) could be well fitted with $\gamma_{LT} = 33(2)$ mJ/mol-K^2 and $\beta_{LT} = 1.31(3)$ mJ/mol-K^4 (Debye temperature $\Theta_D = 181$ K).

On the C_p/T versus T^2 dependence below 4 K, the upturn is observed (see Fig. 5). This upturn is not observed on temperature dependence of C_p (see the inset of Fig. 5). From this, we can conclude that the nature of this rise is not related to the long-range magnetic order of the magnetic moments of Yb. The similar upturn was observed recently in Yb_2AlSi_2 [52]. The upturn could be explained on the basis of the paramagnon model for the spin-fluctuation compounds [53,54].

The evolution of the anomaly at the specific heat versus external magnetic field was studied for the fields in the range 0–9 T (see Fig. 6). The temperature position and specific-heat jump of the anomaly are weakly dependent on the magnetic field. The entropy associated with the anomaly also remains almost unchanged. The Sommerfeld coefficient is slightly reduced for $H \geqslant 6$ T and is equal to $\gamma_{HT} = 146$ mJ/mol-K^2 at $H = 9$ T, which points to the independence of the electronic density of states (DOS) on the magnetic field.

To study the possible occurrence of magnetic transition in $YbNiC_2$, we have measured powder neutron diffraction patterns at $T = 1.3$–100 K, paying attention to the behavior below 20 K. The refinement of the diffraction pattern obtained at $T = 100$ K confirmed that $YbNiC_2$ crystallizes in the orthorhombic $CeNiC_2$-type crystal structure. The refinement also revealed the presence of about 5 wt.% of YbO [55,56]. However, we did not find additional magnetic satellites on the low-temperature patterns, while the intensities of the nuclear peaks were approximately temperature independent.

To search for a possible long-period magnetic order with a periodicity larger than what can be resolved by means of thermal NPD, i.e., the modulated magnetic structure with a period above 30 Å, we have used SANS. Neutron wavelength was set to 4 Å, with sample-to-detector distances of 2, 6.8, and 18.2 m, respectively. The scattering function $S(Q)$ of $YbNiC_2$ was thus recorded for the $4.5 \times 10^{-3} < Q < 3.3 \times 10^{-1}$ Å^{-1} momentum transfer range (Fig. 7). The small Q part of $S(Q)$ follows a Porod law, characteristic of smooth (nuclear and magnetic) interfaces. At the largest Q, $S(Q)$ is best described using a Lorentzian shape, suggesting

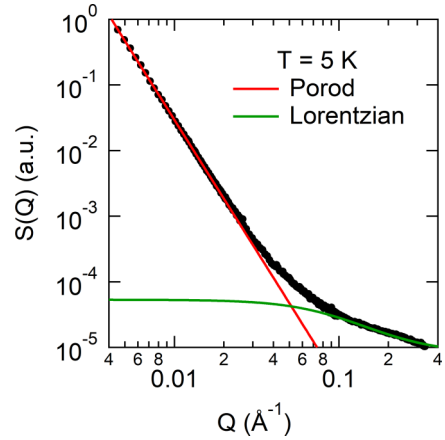

FIG. 7. Ambient-pressure small-angle scattering function $S(Q)$ of $YbNiC_2$ at $T = 5$ K (black points). The red (blue) lines are fits of Porod (Lorentzian) functions to the data, as described in the text.

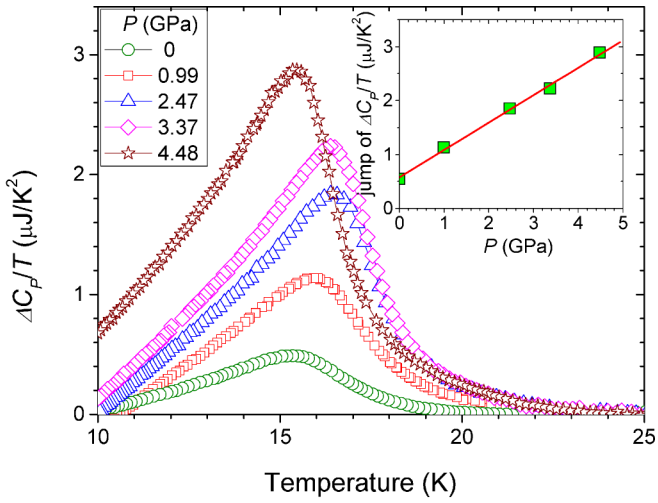

FIG. 8. The temperature dependence of the specific-heat jump $\Delta C_P/T$ of $YbNiC_2$ at high pressures measured in Toroid high-pressure cell. Inset: The C_P/T jump versus pressure.

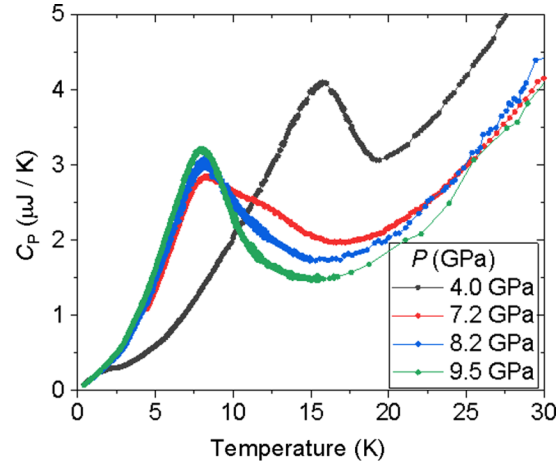

FIG. 9. The temperature dependence of specific heat of $YbNiC_2$ at high pressures measured in Bridgman anvils.

short-range ferromagnetic fluctuations, with a correlation length not exceeding ≈11 Å.

The absence of magnetic Bragg scattering in the SANS and NPD data gives us reason to assume the absence of long-range magnetic ordering at ambient pressure in $YbNiC_2$. However, the possibility of the existence of a low value of the magnetic moment of Yb ions, which are in an intermediate valent state and screened by Kondo effects, requires additional studies of the possibility of the appearance of a long-range magnetic order at low temperatures sufficient to convince its existence.

Based on the presented results, we conclude that the anomaly observed on the temperature dependence of the specific heat is not connected with a magnetic order in the single-phase $YbNiC_2$. We assume that the anomaly is due to a sharp valence change that occurs near the temperature $T_v = 16$ K. This assumption is confirmed by the high-pressure properties and *ab initio* calculations. A discussion of the premises that led us to this conclusion will be given in the Sec. VI.

IV. HIGH-PRESSURE PROPERTIES

To study the specific-heat anomaly and the influence of high pressure in detail, we have performed the specific-heat and resistance measurements.

For the pressures in the range 0–4.5 GPa, the temperature position of the specific-heat anomaly changes non monotonically with pressure. A weak increase of the temperature of this anomaly is observed for $P < 2.5$ GPa, after which it decreases down to 15.5 K at $P = 4.5$ GPa. The specific-heat jump $\Delta C_P/T$ and entropy associated with the anomaly increase linearly with pressure (Fig. 8).

The measurements of specific heat up to 9.5 GPa are performed with Bridgman anvils for the generation of high pressure (Fig. 9). At 4 GPa the shape and the position of the specific-heat anomaly agree well with that found in Toroid-cell measurements (Fig. 8). However, at 7.2 GPa the anomaly has a higher temperature shoulder and can be regarded as having a two-peak structure. One can consider a shoulder (higher temperature peak with small amplitude) at $T \approx 13$ K as a signature of the same transition which manifests itself at $T \approx 15$ K and 4 GPa. The amplitude and position of the second (main) peak at $T \approx 7.5$ K are nearly pressure independent between 7.2 and 9.5 GPa. Note that the shoulder becomes hardly visible at 8.2 GPa and is absent at 9.5 GPa. This picture, consistent with another transition, is distinct from that found at ambient and moderate pressures within the intermediate region between ≈7 and 8 GPa where two low-temperature phases coexist.

The heat-capacity jump ΔC_P associated with the anomaly at $P = 9.5$ GPa is about 2.5 times larger than the jump at $P = 4$ GPa. Comparing it with the jump at $P = 0$ GPa with the help of results of the specific-heat measurements in Toroid high-pressure cell gives the value $\Delta C_P \approx 13.2$ J/mol-K at $P = 9.5$ GPa. The value could be compared with theoretical assessments of the specific-heat jump at long-range magnetic transition with amplitude modulation (AM) $\Delta C_{AM} = 13.4$ J/mol-K and equal amplitudes (EM) $\Delta C_{EM} = 20.2$ J/mol-K magnetic moments structures [57]. The value of ΔC_{AM} is comparable with the experimental specific-heat jump, which suggests a pressure-induced magnetic ordering taking place at $P_C \approx 7.5$ GPa.

Additional measurements of specific heat were performed down to 0.4 K at 4, 8.2, and 9.5 GPa. The upturn of C/T below 4 K clearly visible at ambient pressure (Fig. 5) becomes even more pronounced at 4 GPa, but practically disappears at 8.2 and 9.5 GPa when a new peak at 7.5 K appears. One may suppose that the spin fluctuations in $YbNiC_2$ at ambient and moderate pressures are related to the precursor of ordered magnetic phase above 8 GPa.

The electrical resistance in the pressure range 4–9 GPa below room temperature retains a metallic character [see Fig. 10(c)]. For $P \leqslant 5$ GPa, the metallic character is conserved down to 40 K where the increase of resistance due to the Kondo scattering begins to dominate [see the inset of Fig. 10(a)]. The resistivity maximum temperature T_{max} is weakly pressure dependent up to 10 GPa [see inset of Fig. 10(a)], but the logarithmic contribution to the resistance

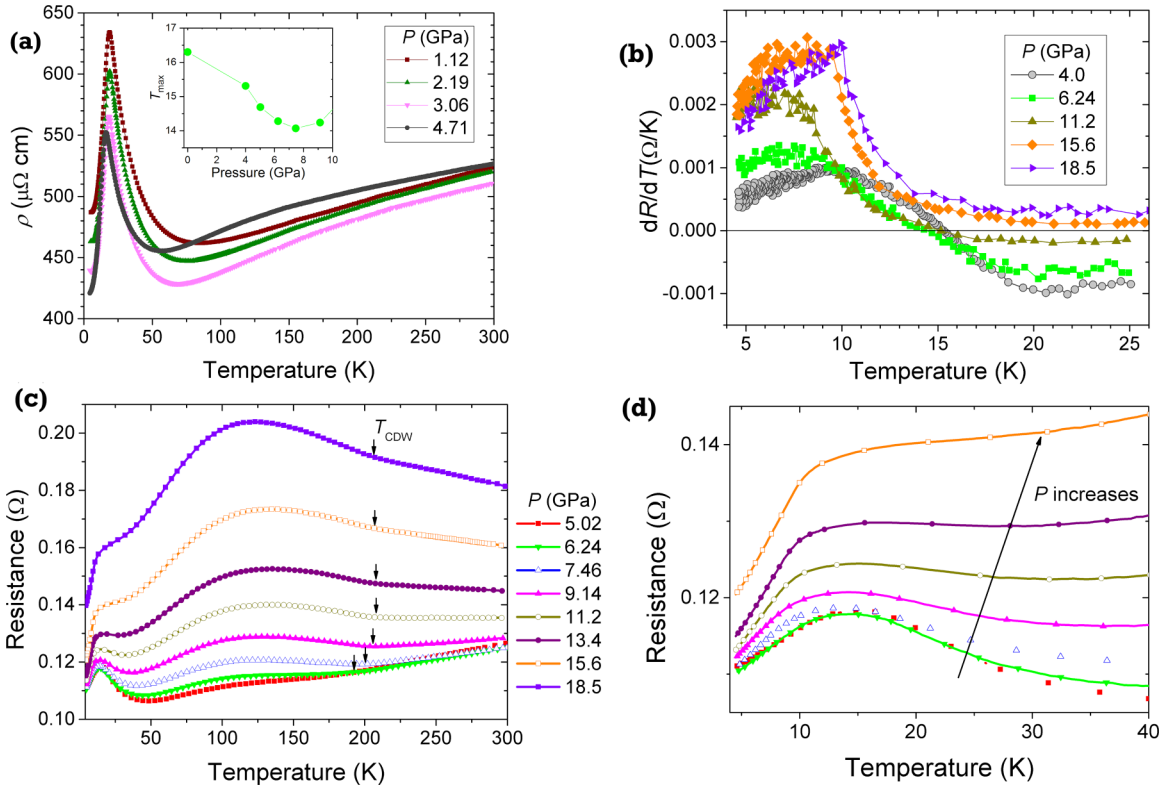

FIG. 10. (a) Temperature dependence of the resistivity for $P = 1.1 - 4.7$ GPa measured in Toroid high-pressure cell. The inset: Resistance maximum temperature versus pressure. (b) Temperature dependence of the derivative of the resistance for $P = 4 - 18.5$ GPa. (c) Temperature dependence of the resistance for $P = 5 - 18.5$ GPa measured in diamond anvil high-pressure cell. (d) The low temperature part of the resistance for $P = 5 - 15.6$ GPa.

is decreased with pressure. Above 13.4 GPa, the Kondo-like behavior is not observed.

Above 5 GPa there is a hump in the temperature dependence of the resistance. The hump shape implies the CDW formation found in many $R\mathrm{NiC_2}$ compounds. The CDW transition temperature T_{CDW} determined from the high temperature onset is increased with pressure from 190 K at $P = 5$ GPa to 208 K at $P = 11.2$ GPa. In the range of pressures 11.2–24.3 GPa, the onset of T_{CDW} is practically pressure independent. The $R(T)$ dependencies obtained at cooling and warming exhibit a hysteresis with $\Delta T \approx 10$ K in the region of T_{CDW}. Similar hystereses at CDW transitions were observed in other $\mathrm{RNiC_2}$ compounds (where $R =$ Y, Lu, Gd, Tb). It can be related to incommensurate-commensurate CDW transition.

Above 13.4 GPa the resistance increases with temperature lowering below room temperature [see Fig. 10(c)]. Such behavior could be attributed to the existence of one more CDW transition above room temperature. From the dependence of T_{CDW} versus the unit cell volume of $R\mathrm{NiC_2}$ series presented in [35], it can be assumed that the CDW in $\mathrm{YbNiC_2}$ is formed at $T_{\mathrm{CDW}}^{\mathrm{HT}} \approx 410$ K. $T_{\mathrm{CDW}}^{\mathrm{HT}}$ affected by pressure and the gap formation during the CDW transition could give a contribution to the resistance.

The low-temperature decrease of the resistance above 7 GPa has a sharper shape in comparison with the decrease at lower pressure below T_{max} [(see Figs. 10(a), 10(c) and 10(d)]. The sharp decrease is similar to the one observed at magnetic transition in other $\mathrm{RNiC_2}$ compounds. This statement can be confirmed by a comparison of the results of numerical differentiation of $R(T)$ obtained at different pressures [see Fig. 10(b)]. For example, $dR(T)/dT$ obtained at 4 and 6.2 GPa passes through zero at T_{max} near 15 K and has the maximum slope just below T_{max}. The temperature where this maximum slope of $dR(T)/dT$ is observed correlates well with the transition temperature obtained from thermodynamic measurements (specific heat). At 11.2, 15.6, and 18.5 GPa, the shape of $dR(T)/dT$ changes. The maximum slope of these dependencies is close to the peak values of dR/dT and again, these points correlate with the transition temperatures determined from specific heat. The higher the pressure the better the shape of $dR(T)/dT$ resembles the λ-shape of $C(T)$ dependence near the magnetic transition.

V. *AB INITIO* CALCULATIONS

A. Method

Our *ab initio* simulations of electronic properties of $\mathrm{YbNiC_2}$ were based on the density functional theory (DFT) with local density approximation (LDA) for the exchange-correlation potential. We used the relativistic APW + lo method with the spin-orbit coupling (SOC) included in a second variational step, as implemented in the Wien2k package [58]. The muffin-tin radii of Yb, Ni, and C were set to 2.50, 1.93, and 1.25 a.u., respectively. Our chosen convergence factor $R_{\mathrm{min}}K_{\mathrm{max}} = 7.5$ corresponded to the plane-wave cut-off parameter of about 500 eV. This, together with the reciprocal

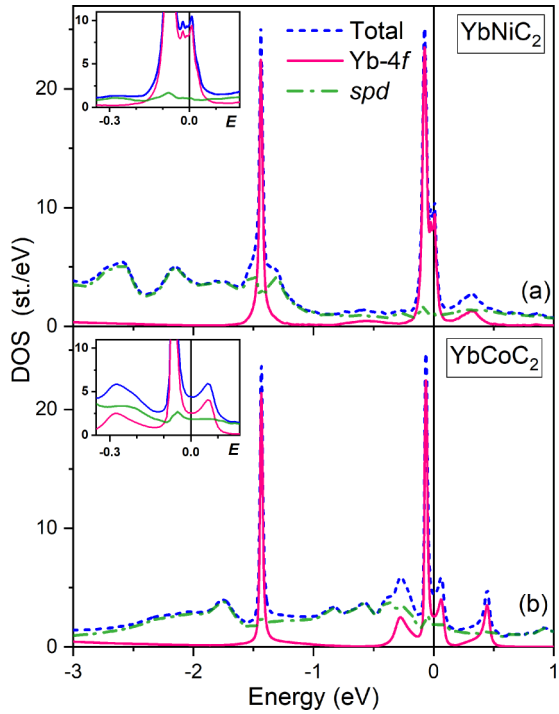

FIG. 11. DMFT-calculated total (dashed blue lines) and $4f$-projected (pink lines) DOS for $YbNiC_2$ (a) in comparison with $YbCoC_2$ (b). The Fermi energy (the vertical line) is set to zero. Insets: The enlarged parts of DOS near the Fermi energy.

space resolution of $2\pi \times 0.03$ Å^{-1} employed to sample the Brillouin zone ensured the total energy convergence of about 10^{-7} eV. The calculations were made at experimental lattice constants found in this work. Starting from the experimental atomic positions, we did the geometry relaxation until the residual atomic forces were converged down to 5 meV/Å. The $4f$ electrons of Yb were explicitly treated as valent and as such were allowed to be not completely localized and hybridize with itinerant states.

To treat the electronic correlation effects more adequately, we employed the combination of DFT-LDA [58] and dynamical mean field theory (DMFT) [59,60] as implemented in the eDMFT package [61–63]. The continuous-time quantum Monte Carlo (QMC-DMFT) impurity solver [64] was employed. Our main DFT + DMFT calculations were performed at 300 K, that is, for the paramagnetic state of $YbNiC_2$. The correlations in the $4f$- and $3d$-electron shells were taken into account. Similar calculations for $YbCoC_2$ were also made for comparison. Getting ahead, we mention that the additional allowance for correlated $3d$ electrons did not reveal any essential difference from the case of correlated $4f$ electrons alone.

B. Results

Figures 11(a) and 11(b) present the DOS for $YbNiC_2$ and $YbCoC_2$, respectively, calculated within the DFT + DMFT approach. The Yb-4f and total ($=4f + spd$) DOSs are shown. For both compounds, the total DOS in the energy range of interest is dominated mainly by the $4f$ and d ($= 3d + 5d$) states, the latter predominantly originating from the transition-metal $3d$ shell. As is seen in the figures, the two compounds are metallic and the Fermi energy, E_F, is at a local minimum near a very steep slope of the high $4f$ peak.

Our estimate for the total DOS (dashed blue lines in Fig. 11) at the Fermi level, $N(E_F)$, provides 9.6 st./eV for $YbNiC_2$ and a more than twice as low value of 4.5 st./eV for $YbCoC_2$, while for the $4f$ contribution (pink lines) we obtain $N_{4f}(E_F) = 8.5$ and 2.6 st./eV, respectively. However, the ratio of the conduction spd-electron contributions (denoted as c-DOS) for $YbNiC_2$ and $YbCoC_2$ is opposite: $N_c(E_F)$ determined as $N(E_F) - N_{4f}(E_F)$ is equal to 1.1 and 1.9 st./eV, correspondingly. Note that due to the proximity of the $4f$ peak, $N(E_F)$ is very sensitive to the calculation accuracy and small variations of parameters, so this estimate is only indicative.

Comparison of the dashed blue lines in Figs. 11(a) and 11(b) shows that in the case of $YbCoC_2$, there is an appreciable c-DOS around the Fermi energy, which implies strong hybridization of the partially filled $4f$ shell with conduction electrons (predominantly of d character). The c-DOS of $YbNiC_2$, on the other hand, primarily contributed by the more filled (and hence lower-lying and more localized) Ni-$3d$ shell, is mainly concentrated below–1 eV and therefore, the f-c hybridization is less significant for the near-E_F states that govern the electronic properties of metals.

We did several computation runs at different pressures and temperatures. In all these cases the two compounds remain metallic. At normal conditions ($P \approx 0, T = 300$ K), the evaluated number of Yb-$4f$ electrons is equal to 13.06 for $YbCoC_2$ and 13.15 for $YbNiC_2$, that is, the Yb ions in both compounds are in an intermediate-valent state with a valence of 2.94 and 2.85, respectively. This difference of almost 0.1 electron is responsible for different electronic and magnetic properties of the two compounds. In $YbCoC_2$, the Yb ions are closer to the Yb^{3+} state, which, in particular, favors the formation of magnetic order even at normal pressure, as has been shown in our previous paper [29].

Calculations show that at elevated pressures, the Yb valence in $YbNiC_2$ increases to 2.86 at 13 GPa and 2.88 at 37 GPa. This could be intuitively explained by an enhancement in the overlap integrals as the atoms approach each other on compression. A similar trend is observed at normal pressure with increasing temperature: the Yb valence is equal to 2.83, 2.85 and 2.86 at 100, 300, and 1000 K, respectively. This can also be expected due to an increase in the hopping of itinerant charge carriers on heating.

Thus, on compression, the Yb valence in $YbNiC_2$ tends to that of $YbCoC_2$ with its higher f-d bare hybridization responsible for normal-pressure magnetism. This is entirely consistent with our experimental observation (see Sec. IV) that magnetic ordering in $YbNiC_2$ appears only at high pressure.

The band structure (more exactly, the electronic spectral function) and the corresponding FS topology calculated within DFT + DMFT are shown in Figs. 12 and 13 for $YbNiC_2$ and $YbCoC_2$, correspondingly. In the case of $YbCoC_2$, the near-E_F states (predominantly of Co-$3d$ character) form the complex band structure and FS. Some spectral weight incoherence near E_F can be seen in Fig. 13. For $YbNiC_2$ with its low-lying Ni-$3d$ states, only two well-defined quasiparticle bands related to the two spin channels of SOC cross the Fermi energy.

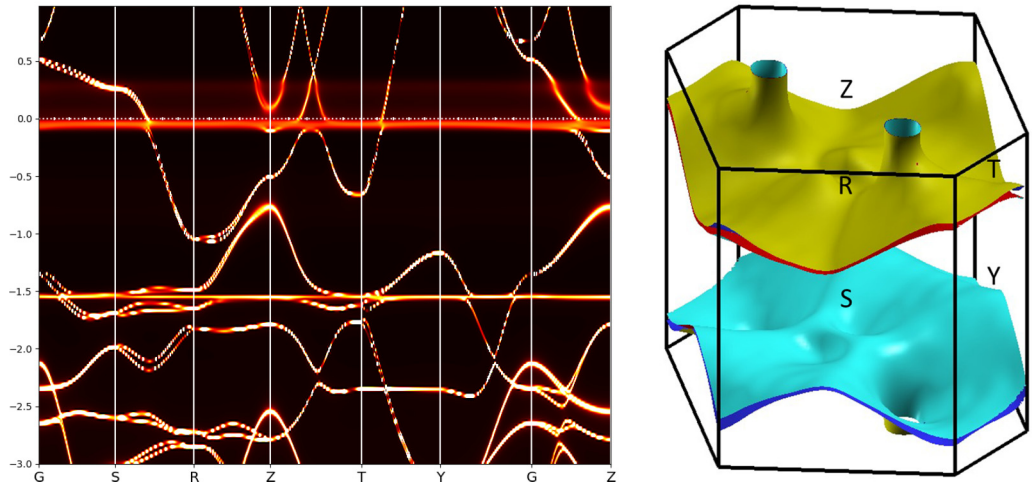

FIG. 12. DMFT-calculated band structure along high-symmetry k path (left) and FS (right) of $YbNiC_2$ at $T = 300$ K. The FS was generated using the XCRYSDEN software [65].

Accordingly, the FS of $YbNiC_2$ is quite simple in shape (Fig. 12). It consists of two quasi-1D-type low-curvature sheets open in the ΓSY (k_x, k_y) plane and connected by nearly 2D cylindrical necks parallel to the ΓZ (k_z) direction. On the contrary, the complex FS of isostructural $YbCoC_2$ formed by several bands is typical of 3D metal. Comparison of the two FS also implies a lower (and more anisotropic) conductivity of $YbNiC_2$ than that of $YbCoC_2$. This anisotropy of conductivity parallel and perpendicular to the k_z direction can be detected in single crystals.

Remarkably, the FS of $YbNiC_2$ is characterized by parallel nearly flat pieces that could be partially nested with appropriate q-vectors, thereby enabling the CDW formation. This confirms qualitatively our experimental observation of the CDW transition in $YbNiC_2$ presented above.

VI. DISCUSSION OF THE RESULTS

We have studied experimentally and theoretically $YbNiC_2$, which is a novel compound displaying the interplay between valence fluctuations, CDW, magnetic, and Kondo interactions. The experimental data and *ab initio* calculations of $YbNiC_2$ underline the importance of the $c - f$ hybridization, the topology of the FS, and the valence-lattice and electron-phonon interactions. Our experimental findings are summarized in the $P - T$ phase diagram shown in Fig. 14.

Data at atmospheric pressure indicate that in $YbNiC_2$, the Kondo lattice is formed. At $T_v = 16$ K (at 0 GPa) there is an anomaly on the temperature dependence of the specific heat which we assign to an abrupt valence transition (crossover) from approximately three-valent to the intermediate valent state of Yb accompanied with enhanced spin fluctuations. T_v decreases with increasing pressure. For $P > P_c \approx 7$ GPa, a stabilization of 3^+ valent state of Yb is observed when the valence transition is suppressed. The intermediate valence state at ambient pressure and the stabilization of nearly 3^+ valent state at high pressure are confirmed by the *ab initio* calculations.

A decrease of the Kondo temperature and interaction strength J between conduction and f electrons with pressure lead to the formation of the magnetic state at $T_m \approx 11$ K. The

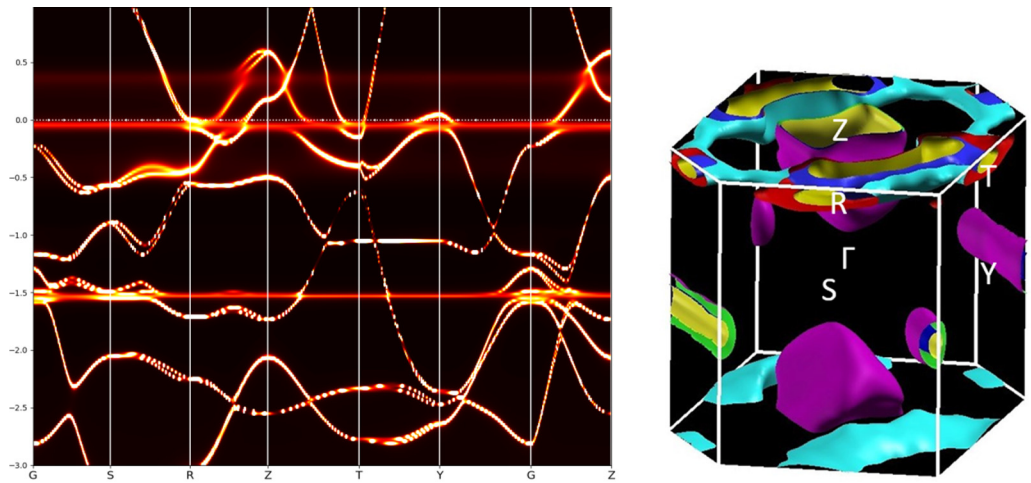

FIG. 13. DMFT-calculated band structure (left) and the FS (right) of $YbCoC_2$ at $T = 300$ K.

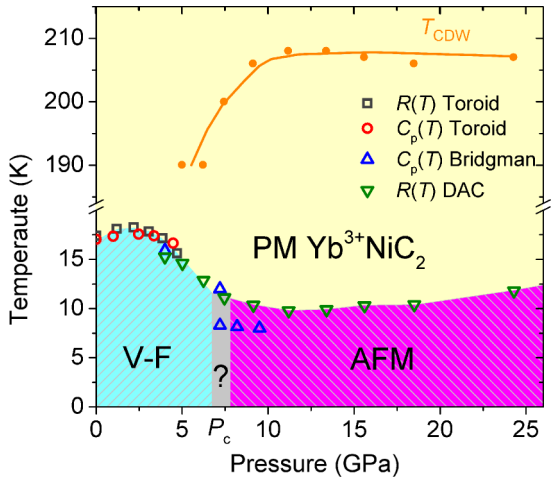

FIG. 14. The $P-T$ phase diagram of $YbNiC_2$. Yellow region (PM), paramagnetic state with Yb^{3+}; blue region (V-F), valence-fluctuating state of Yb ions with enhanced spin-fluctuations; magenta region (AFM), antiferromagnetic Yb; gray region (?), a possible coexistence of V-F and AFM phases; orange points (T_{CDW}), CDW transition temperature (the orange line is a guide to the eye). Gray squares, red circles, and blue and green triangles are the temperatures of anomalies deduced from the measurements of resistance and specific heat.

magnetic transition temperature T_m slightly increases with external pressure as it should be for the magnetic transition temperature in Yb-based HF compounds in the case of a significant concurrency between Kondo and magnetic interactions [7,66–68]. The increase of T_m may be connected with the stabilization of the three-valent magnetic state of Yb. We argue that in the compound the ratio $R = T_{RKKY}/T_K$ close to the critical ration R_{cr} such that for $R > R_{cr}$ the magnetic order is observed. This is confirmed by the weak pressure dependence of $T_{max} \propto T_K$ below P_c and its slight increase above P_c [69] as shown on the inset of Fig. 10(a). However, it should be noted that the value of T_{max} can also be influenced by the crystal field effects and RKKY interaction. The pressure changes the value of R from below R_{cr} at $P < P_c$ to above R_{cr} at higher pressure.

In $YbNiC_2$ the CDW transition was observed at $T \approx 185$ K at $P = 5$ GPa and above. It is nearby the incommensurate-commensurate transition. At high pressure there is also a possibility for another CDW transition at $T > 300$ K. The CDW formation is qualitatively confirmed by the quasi-1D shape of the FS which consists of two large parallel nearly flat sheets that can be partially nested.

The comparison of our *ab initio* results for $YbNiC_2$ with isostructural $YbCoC_2$ revealed a significant difference between these two compounds. In $YbCoC_2$ there is an appreciable density of conduction-electron states near the Fermi energy, which are hybridized with a delocalized part of $4f$ states also situated in this energy range. In $YbNiC_2$, the transition-metal $3d$ shell is more filled and hence the $3d$ electrons are deeper in energy and more localized. This means that, compared to $YbCoC_2$, they are less involved in conductivity and indirect RKKY exchange. That is because the strength of the RKKY interaction strongly depends on the susceptibility of conduction electrons located near Fermi level [70]. The shape of the calculated FS implies a low and highly anisotropic conductivity of $YbNiC_2$.

It should be noted that the obtained phase diagram (Fig. 14) usually observed for Eu-based intermetallic systems while Ce- and Yb-based systems often have a quantum critical point [71–73] with a possible occurrence of a superconducting dome. The range of Eu-based compounds undergoes sharp valence transitions. In these compounds the Eu valence change dramatically in comparison with the most Ce- and Yb-based compounds in the same temperature region [74,75]. Usually, the FOVT transition is observed in such systems [76,77]. The phase diagram of $YbNiC_2$ also has a form similar to the well-known $YbInCu_4$ compound mentioned in Sec. I.

Some details of transition near P_c remain unresolved. From the available experimental measurements, it can be assumed that the magnetic transition is of first-order type (see Fig. 14). A similar situation was analyzed in Ref. [10], where it was shown that the enhanced valence fluctuations can suppress the magnetic order at $T \approx 0$ K. This can lead to the first-order magnetic transitions in some HF compounds. However, for the $YbNiC_2$ compound, elucidation of the type of magnetic transition requires additional measurements at high pressure by various methods, such as neutron spectroscopy, or local probe techniques, such as Muon spin spectroscopy, Mossbauer spectroscopy, time differential perturbed angular correlation under high pressure. The type of magnetism in $YbNiC_2$ at high pressure also remains unclear. $CeNiC_2$ and $YbCoC_2$ are known to order antiferromagnetically at ambient pressure [29,78]. $ErNiC_2$ and $TmNiC_2$ which also order antiferromagnetically have the transitions temperatures which approximately correspond to that in $YbNiC_2$ at P_c [39]. On the other hand, as it was shown in Ref. [79], the NC compounds could prefer the FM order in Kondo lattices due to the existence of an extended s-wave RKKY interaction.

At the present time the value of Yb valence in $YbNiC_2$ is determined only from the *ab initio* calculations. It is known that valence determined in such a way presents a good assessment [80,81], but we were not able to detect Yb valence transition in our calculations. The temperature and pressure dependence of Yb valence requires additional studies. In the future, we plan to study the pressure dependence of Yb valence in $YbNiC_2$ in detail by means of x-ray absorption techniques [82] which will allow us to understand the microscopic nature of unusual behavior in the compound and the region of coexistence of V-F and AFM phases (the gray region in Fig. 14).

ACKNOWLEDGMENTS

The authors acknowledge useful discussions with A.V. Nikolaev. N.M.C. and M.V.M. gratefully thank G.L. Pascut for his technical advice on the DMFT calculations. This work was supported by Russian Science Foundation: D.A.S., V.A.S., A.E.P. and A.V.T. acknowledge the support of their experimental work (Grant RSF 17-12-01050); N.M.C. and M.V.M. are grateful for the support of their theoretical work (Grant RSF 18-12-00438). The numerical calculations were carried out using computing resources of the federal collective usage center Complex for Simulation and Data Processing for Mega-science Facilities at NRC "Kurchatov Institute" [83],

the "Govorun" supercomputer of the Multifunctional Information and Computing Complex at LIT JINR (Dubna), and supercomputers at Joint Supercomputer Center of RAS (JSCC RAS).

[1] P. Gegenwart, Q. Si, and F. Steglich, Nat. Phys. **4**, 186 (2008).
[2] J. L. Sarrao, A. P. Ramirez, T. W. Darling, F. Freibert, A. Migliori, C. D. Immer, Z. Fisk, and Y. Uwatoko, Phys. Rev. B **58**, 409 (1998).
[3] M. S. Torikachvili, S. Jia, E. D. Mun, S. T. Hannahs, R. C. Black, W. K. Neils, D. Martien, S. L. Bud'ko, and P. C. Canfield, Proc. Natl. Acad. Sci. USA **104**, 9960 (2007).
[4] K. Kummer, C. Geibel, C. Krellner, G. Zwicknagl, C. Laubschat, N. B. Brookes, and D. V. Vyalikh, Nat. Commun. **9**, 2011 (2018).
[5] Z. F. Weng, M. Smidman, L. Jiao, X. Lu, and H. Q. Yuan, Rep. Prog. Phys. **79**, 094503 (2016).
[6] N. Tsujii and H. Kitazawa, Solid State Commun. **159**, 65 (2013).
[7] K. Matsubayashi, T. Hirayama, T. Yamashita, S. Ohara, N. Kawamura, M. Mizumaki, N. Ishimatsu, S. Watanabe, K. Kitagawa, and Y. Uwatoko, Phys. Rev. Lett. **114**, 086401 (2015).
[8] Z. Fisk and M. Maple, J. Alloys Compd. **183**, 303 (1992).
[9] D. Braithwaite, A. Fernandez-Pañella, E. Colombier, B. Salce, G. Knebel, G. Lapertot, V. Balédent, J.-P. Rueff, L. Paolasini, R. Verbeni *et al.*, J. Supercond. Novel Magn. **26**, 1775 (2013).
[10] S. Watanabe and K. Miyake, J. Phys.: Condens. Matter **23**, 094217 (2011).
[11] F. Stegemann, J. Stahl, M. Bartsch, H. Zacharias, D. Johrendt, and O. Janka, Chem. Sci. **10**, 11086 (2019).
[12] K. Matsubayashi, N. Kawamura, M. Mizumaki, and N. Ishimatsu, High Press. Res. **36**, 419 (2016).
[13] I. Felner, I. Nowik, D. Vaknin, U. Potzel, J. Moser, G. M. Kalvius, G. Wortmann, G. Schmiester, G. Hilscher, E. Gratz *et al.*, Phys. Rev. B **35**, 6956 (1987).
[14] J. M. Lawrence, P. S. Riseborough, and R. D. Parks, Rep. Prog. Phys. **44**, 1 (1981).
[15] J.-P. Rueff, J.-P. Itié, M. Taguchi, C. F. Hague, J.-M. Mariot, R. Delaunay, J.-P. Kappler, and N. Jaouen, Phys. Rev. Lett. **96**, 237403 (2006).
[16] E. Annese, A. Barla, C. Dallera, G. Lapertot, J.-P. Sanchez, and G. Vankó, Phys. Rev. B **73**, 140409(R) (2006).
[17] T. Mito, T. Koyama, S. Wada, T. Muramatsu, T. C. Kobayashi, and J. L. Sarrao, J. Magn. Magn. Mater. **272-276**, E47 (2004).
[18] M. Ito, S. Sakamoto, K. Asada, T. Fujita, K. Kojima, K. Hiraoka, and T. Suzuki, J. Magn. Magn. Mater. **272-276**, E37 (2004).
[19] T. Mito, M. Nakamura, M. Otani, T. Koyama, S. Wada, M. Ishizuka, M. K. Forthaus, R. Lengsdorf, M. M. Abd-Elmeguid, and J. L. Sarrao, Phys. Rev. B **75**, 134401 (2007).
[20] H. Yamaoka, I. Jarrige, N. Tsujii, J.-F. Lin, T. Ikeno, Y. Isikawa, K. Nishimura, R. Higashinaka, H. Sato, N. Hiraoka *et al.*, Phys. Rev. Lett. **107**, 177203 (2011).
[21] T. Mazet, H. Ihou-Mouko, D. H. Ryan, C. J. Voyer, J. M. Cadogan, and B. Malaman, J. Phys.: Condens. Matter **22**, 116005 (2010).
[22] L. Eichenberger, A. Magnette, D. Malterre, R. Sibille, F. Baudelet, L. Nataf, and T. Mazet, Phys. Rev. B **101**, 020408(R) (2020).
[23] A. Magnette, A. Verniere, G. Venturini, L. Eichenberger, B. Malaman, and T. Mazet, J. Magn. Magn. Mater. **458**, 19 (2018).
[24] E. Bauer, R. Hauser, A. Galatanu, H. Michor, G. Hilscher, J. Sereni, M. G. Berisso, P. Pedrazzini, M. Galli, F. Marabelli *et al.*, Phys. Rev. B **60**, 1238 (1999).
[25] K. Yamamoto, H. Yamaoka, N. Tsujii, A. Mihai Vlaicu, H. Oohashi, S. Sakakura, T. Tochio, Y. Ito, A. Chainani, and S. Shin, J. Phys. Soc. Jpn. **76**, 124705 (2007).
[26] E. Bauer, L. Tuan, R. Hauser, E. Gratz, T. Holubar, G. Hilscher, H. Michor, W. Perthold, C. Godart, E. Alleno *et al.*, Phys. Rev. B **52**, 4327 (1995).
[27] T. Tanaka and Y. Kubo, J. Phys. Soc. Jpn. **79**, 124710 (2010).
[28] D. Andreica, A. Amato, F. N. Gygax, and A. Schenck, J. Phys.: Condens. Matter **15**, 6997 (2003).
[29] D. A. Salamatin, N. Martin, V. A. Sidorov, N. M. Chtchelkatchev, M. V. Magnitskaya, A. E. Petrova, I. P. Zibrov, L. N. Fomicheva, J. Guo, C. Huang *et al.*, Phys. Rev. B **101**, 100406(R) (2020).
[30] J. F. Landaeta, D. Subero, P. Machado, F. Honda, and I. Bonalde, Phys. Rev. B **96**, 174515 (2017).
[31] G. Prathiba, I. Kim, S. Shin, J. Strychalska, T. Klimczuk, and T. Park, Sci. Rep. **6**, 26530 (2016).
[32] F. Morales, L. F. Mendivil, and R. Escamilla, J. Phys.: Condens. Matter **26**, 455602 (2014).
[33] S. Shimomura, C. Hayashi, G. Asaka, N. Wakabayashi, M. Mizumaki, and H. Onodera, Phys. Rev. Lett. **102**, 076404 (2009).
[34] N. Yamamoto, R. Kondo, H. Maeda, and Y. Nogami, J. Phys. Soc. Jpn. **82**, 123701 (2013).
[35] M. Roman, J. Strychalska-Nowak, T. Klimczuk, and K. K. Kolincio, Phys. Rev. B **97**, 041103(R) (2018).
[36] S. Steiner, H. Michor, O. Sologub, B. Hinterleitner, F. Hofenstock, M. Waas, E. Bauer, B. Stoger, V. Babizhetskyy, V. Levytskyy *et al.*, Phys. Rev. B **97**, 205115 (2018).
[37] M. Roman, L. Litzbarski, T. Klimczuk, and K. K. Kolincio, Phys. Rev. B **99**, 245152 (2019).
[38] A. D. Hillier, J. Quintanilla, and R. Cywinski, Phys. Rev. Lett. **102**, 117007 (2009).
[39] W. Schafer, W. Kockelmann, G. Will, J. Yakinthos, and P. Kotsanidis, J. Alloys Compd. **250**, 565 (1997).
[40] W. Schafer, G. Will, J. Yakinthos, and P. Kotsanidis, J. Alloys Compd. **180**, 251 (1992).
[41] P. Kotsanidis, J. Yakinthos, and E. Gamari-Seale, J. Less-Common Met. **152**, 287 (1989).
[42] A. Tsvyashchenko, J. Less-Common Met. **99**, L9 (1984).
[43] F. Bouquet, Y. Wang, H. Wilhelm, D. Jaccard, and A. Junod, Solid State Commun. **113**, 367 (2000).
[44] V. A. Sidorov, J. D. Thompson, and Z. Fisk, J. Phys.: Condens. Matter **22**, 406002 (2010).

[45] A. E. Petrova, V. A. Sidorov, and S. M. Stishov, Phys. B: Condens. Matter **359-361**, 1463 (2005).

[46] H. K. Mao, J. Xu, and P. M. Bell, J. Geophys. Res.: Solid Earth **91**, 4673 (1986).

[47] G. Chaboussant, S. Désert, P. Lavie, and A. Brûlet, J. Phys.: Conf. Ser. **340**, 012002 (2012).

[48] J. Rodriguez-Carvajal, Phys. B: Condens. Matter **192**, 55 (1993).

[49] W. Jeitschko and M. Gerss, J. Less-Common Met. **116**, 147 (1986).

[50] J. Hodges, P. Bonville, and M. Ocio, Eur. Phys. J. B **57**, 365 (2007).

[51] Y. Long, C. Z. Zheng, J. L. Luo, Z. J. Cheng, and Y. S. He, J. Appl. Phys. **89**, 3523 (2001).

[52] K. V. Shah, P. Bonville, P. Manfrinetti, F. Wrubl, and S. K. Dhar, J. Phys.: Condens. Matter **21**, 176001 (2009).

[53] S. K. Dhar, K. A. Gschneidner, W. H. Lee, P. Klavins, and R. N. Shelton, Phys. Rev. B **36**, 341 (1987).

[54] T. Takabatake, M. Ishikawa, and T. Satoh, Solid State Commun. **59**, 673 (1986).

[55] R. M. Moon, W. C. Koehler, H. R. Child, and L. J. Raubenheimer, Phys. Rev. **176**, 722 (1968).

[56] A. Werner, H. Hochheimer, A. Jayaraman, and J. Leger, Solid State Commun. **38**, 325 (1981).

[57] J. A. Blanco, D. Gignoux, and D. Schmitt, Phys. Rev. B **43**, 13145 (1991).

[58] P. Blaha, K. Schwarz, G. Madsen, D. Kvasnicka, J. Luitz, R. Laskowski, F. Tran, and L. Marks, *WIEN2k, An Augmented Plane Wave + Local Orbitals Program for Calculating Crystal Properties* (Karlheinz Schwarz, Techn. Universitat Wien, Austria, 2018).

[59] A. Georges, G. Kotliar, W. Krauth, and M. J. Rozenberg, Rev. Mod. Phys. **68**, 13 (1996).

[60] G. Kotliar, S. Y. Savrasov, K. Haule, V. S. Oudovenko, O. Parcollet, and C. A. Marianetti, Rev. Mod. Phys. **78**, 865 (2006).

[61] K. Haule, C.-H. Yee, and K. Kim, Phys. Rev. B **81**, 195107 (2010).

[62] K. Haule, available at http://hauleweb.rutgers.edu.

[63] K. Haule and T. Birol, Phys. Rev. Lett. **115**, 256402 (2015).

[64] K. Haule, Phys. Rev. B **75**, 155113 (2007).

[65] A. Kokalj, Comput. Mater. Sci. **28**, 155 (2003).

[66] H. Q. Yuan, M. Nicklas, Z. Hossain, C. Geibel, and F. Steglich, Phys. Rev. B **74**, 212403 (2006).

[67] G. Spam, J. Thompson, and A. Hamzic, J. Alloys Compd. **181**, 197 (1992).

[68] Y. Saiga, K. Matsubayashi, T. Fujiwara, M. Kosaka, S. Katano, M. Hedo, T. Matsumoto, and Y. Uwatoko, J. Phys. Soc. Jpn. **77**, 053710 (2008).

[69] A. V. Goltsev and M. M. Abd-Elmeguid, J. Phys.: Condens. Matter **17**, S813 (2005).

[70] J. Jensen and A. R. Mackintosh, *Rare Earth Magnetism: Structures and Excitations* (Oxford University Press, New York, 1991).

[71] S. Seiro and C. Geibel, J. Phys.: Condens. Matter **23**, 375601 (2011).

[72] P. Wachter and H. Boppart, Eds., *The phase diagram for a Eu compound undergoing configurational crossover: Mössbauer effect measurements*, in Valence Instabilities, Proceedings of the International Conference (Elsevier Science Ltd, 1982).

[73] C. U. Segre, M. Croft, J. A. Hodges, V. Murgai, L. C. Gupta, and R. D. Parks, Phys. Rev. Lett. **49**, 1947 (1982).

[74] A. Mitsuda, E. Kishaba, T. Fujimoto, K. Oyama, H. Wada, M. Mizumaki, N. Kawamura, and N. Ishimatsu, Phys. B: Condens. Matter **536**, 427 (2018).

[75] K. Ichiki, K. Mimura, H. Anzai, T. Uozumi, H. Sato, Y. Utsumi, S. Ueda, A. Mitsuda, H. Wada, Y. Taguchi *et al.*, Phys. Rev. B **96**, 045106 (2017).

[76] A. Mitsuda, S. Hamano, N. Araoka, H. Yayama, and H. Wada, J. Phys. Soc. Jpn. **81**, 023709 (2012).

[77] F. Honda, K. Okauchi, A. Nakamura, D. Li, D. Aoki, H. Akamine, Y. Ashitomi, M. Hedo, T. Nakama, and Y. Onuki, J. Phys. Soc. Jpn. **85**, 063701 (2016).

[78] K. Motoya, K. Nakaguchi, N. Kayama, K. Inari, J. Akimitsu, K. Izawa, and T. Fujita, J. Phys. Soc. Jpn. **66**, 1124 (1997).

[79] S. Ahamed, R. Moessner, and O. Erten, Phys. Rev. B **98**, 054420 (2018).

[80] E. R. Ylvisaker, J. Kuneš, A. K. McMahan, and W. E. Pickett, Phys. Rev. Lett. **102**, 246401 (2009).

[81] H. Yamaoka, P. Thunström, N. Tsujii, K. Katoh, Y. Yamamoto, E. F. Schwier, K. Shimada, H. Iwasawa, M. Arita, I. Jarrige *et al.*, J. Phys.: Condens. Matter **29**, 475502 (2017).

[82] L. Moreschini, C. Dallera, J. J. Joyce, J. L. Sarrao, E. D. Bauer, V. Fritsch, S. Bobev, E. Carpene, S. Huotari, G. Vankó *et al.*, Phys. Rev. B **75**, 035113 (2007).

[83] http://ckp.nrcki.ru/.